Gigantic transmission band-edge resonance in periodic stacks of anisotropic layers

Alex Figotin and Ilya Vitebskiy

University of California at Irvine, Irvine, California 92697-3875
(Received 23 June 2005; published 29 September 2005)

We consider Fabry-Perot cavity resonance in periodic stacks of anisotropic layers with misaligned in-plane anisotropy at the frequency close to a photonic band edge. We show that in-plane dielectric anisotropy can result in a dramatic increase in field intensity and group delay associated with the transmission resonance. The field enhancement turns out to be proportional to fourth degree of the number N of layers in the stack. By contrast, in common periodic stacks of isotropic layers, those effects are much weaker and proportional to N^2. Thus, the anisotropy allows one to drastically reduce the size of the resonance cavity with similar performance. The key characteristic of the periodic arrays with gigantic transmission resonance is that the dispersion curve $\omega(k)$ at the photonic band edge has the degenerate form $\Delta\omega \sim (\Delta k)^4$, rather than the regular form $\Delta\omega \sim (\Delta k)^2$. This can be realized in specially arranged stacks of misaligned anisotropic layers. The degenerate band-edge cavity resonance with similar outstanding properties can also be realized in a waveguide environment, as well as in a linear array of coupled multimode resonators, provided that certain symmetry conditions are in place.

I. INTRODUCTION

The subject of this paper is the Fabry-Pérot cavity resonance in periodic layered structures. This phenomenon, known for many decades, is also referred to as the *transmission band-edge resonance*, because it occurs in the vicinity of photonic band-edge frequencies in finite photonic crystals and is accompanied by sharp transmission peaks. This basic effect can occur in a finite periodic array of any two alternating materials with different refractive indices. It can also be realized in a waveguide environment, or in a finite array of coupled resonators. The only essential requirements are (a) low absorption, (b) the appropriate number N of unit cells in the periodic array, and (c) the presence of a frequency gap (a stop band) in the frequency spectrum of the periodic array. The latter is a universal property of almost any lossless spatially periodic structure. This phenomenon has found numerous and diverse practical applications in optics. Below we briefly outline some basic features of the classical band-edge resonance in periodic stacks of isotropic layers. We highlight only those points that are necessary for the following comparative analysis of stacks involving anisotropic layers. More detailed information on the relevant aspects of electrodynamics of layered dielectric media can be found in an extensive literature on the subject (see, for example, [1–9], and references therein).

Consider a simplest periodic array of alternating dielectric layers A and B, as shown in Fig. 1(a). The layers are made of transparent isotropic materials with different refractive indices n_A and n_B. Such periodic stacks are also referred to as one-dimensional photonic crystals. The electromagnetic eigenmodes of the periodic structure in Fig. 1(a) are Bloch waves with a typical wave number–frequency diagram shown in Fig. 1(b).

Consider now a finite periodic stack composed of N unit cells L in Fig. 1(a). Such a stack is commonly referred to as a Fabry-Pérot cavity. If the number N of the double layers L is significant, the stack periodicity causes coherent interfer-

ence of light scattered by the layers interfaces. In practice, periodic stacks having as few as several periods L can display almost total reflectivity at the band-gap frequencies, provided that the refractive indices n_A and n_B of the adjacent layers differ significantly.

A typical frequency dependence of the finite stack transmittance is presented in Fig. 2. The frequency range shown includes the vicinity of the photonic band edge (BE) g in Fig. 1(b). The sharp transmission peaks below the photonic band-edge frequency ω_g correspond to transmission band-edge resonances, also known as Fabry-Pérot cavity resonances. At each resonance, the electromagnetic field inside the periodic stack is close to a standing wave composed of a forward and a backward Bloch eigenmode with large and nearly equal amplitudes. The slab boundaries coincide with the standing wave nodes, where the forward and backward Bloch components interfere destructively, as illustrated in Figs. 3 and 4. The latter circumstance determines the wave numbers of the
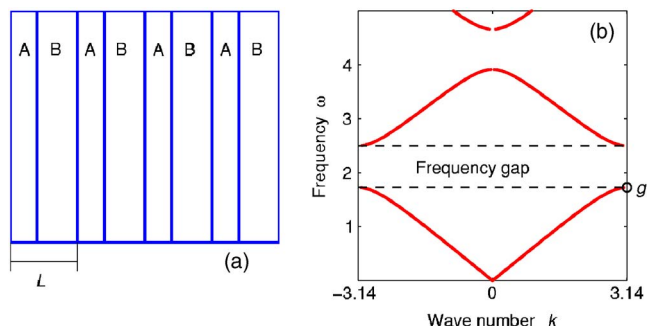

FIG. 1. (Color online) (a) Periodic stack composed of two alternating layers A and B, each of which is made of isotropic transparent material. L is the unit cell of the periodic structure. The physical characteristics of the stack are specified in the Appendix. (b) The corresponding k-ω diagram. The wave number k and the frequency ω are expressed in units of $1/L$ and c/L. The point g at the Brillouin zone boundary designates the edge of the lowest frequency band.
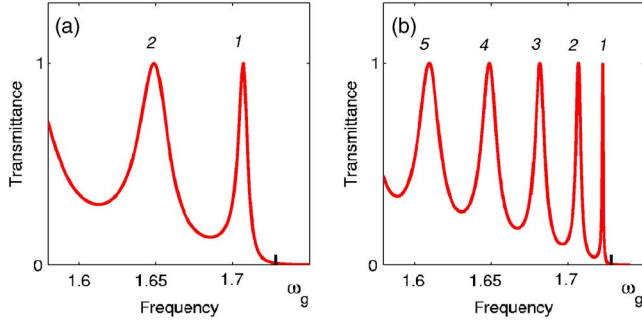
FIG. 2. (Color online) Typical transmission spectrum of finite periodic stacks composed of different numbers N of unit cells L shown in Fig. 1. The sharp transmission peaks below the band-edge frequency ω_g are associated with photonic band-edge resonance. $N=$ (a) 16 and (b) 32.

forward and backward Bloch components at the resonance frequencies

$$k_s \approx k_g \pm \frac{\pi}{NL} s, \quad s = 1, 2, \ldots, \tag{1}$$

where s is the order number of the resonant peak in Fig. 2, and k_g is the wave number corresponding to the photonic band edge. In our case, $k_g = \pi/L$. The resonance frequencies themselves can be expressed in terms of the dispersion relation $\omega(k)$ of the corresponding frequency band. Indeed, just below the photonic band edge g in Fig. 1(b), the dispersion relation $\omega(k)$ can be approximated by the quadratic parabola

$$\omega \approx \omega_g + \frac{\omega_g''}{2}(k - k_g)^2 \quad \text{where } \omega_g'' = \left(\frac{\partial^2 \omega}{\partial k^2}\right)_{k=k_g} < 0. \tag{2}$$

This relation together with (1) yield the frequencies of the resonant transmission peaks in Fig. 2:

$$\omega_s(N) \approx \omega_g + \frac{\omega_g''}{2}\left(\frac{\pi}{NL} s\right)^2, \quad s = 1, 2, \ldots, \tag{3}$$

where $\omega_g = \omega(k_g)$ is the band-edge frequency. For example, the transmission peak 1 closest to the photonic band edge is located at
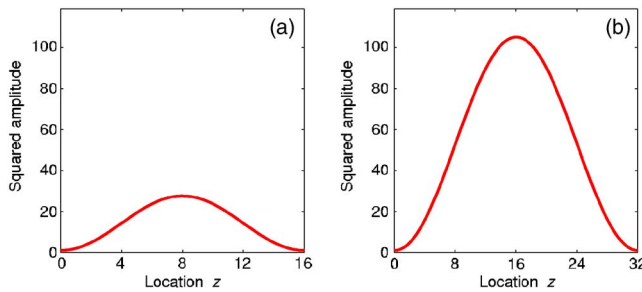

FIG. 3. (Color online) Smoothed intensity distribution (A3) iside periodic stack at the frequency $\omega_1(N)$ in Eq. (4) of the first transmission resonance. The amplitude of the incident wave is unity. The distance z from the left boundary is expressed in units of L. At the stack boundaries at $z=0$ and NL, the field intensity is of the order of unity, while inside the slab it is enhanced by factor N^2. $N=$ (a) 16 and (b) 32.
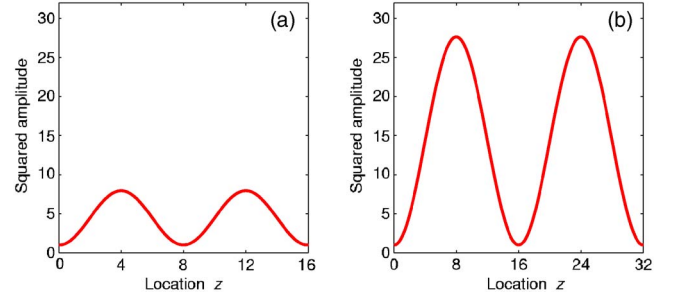

FIG. 4. (Color online) The same as in Fig. 3, but at the frequency $\omega_2(N)$ in Eq. (3) of the second transmission resonance in Figs. 2(a) and 2(b), respectively.

$$\omega_1(N) \approx \omega_g + \frac{\omega_g''}{2}\left(\frac{\pi}{NL}\right)^2. \tag{4}$$

The dependence (3) is illustrated in Fig. 2.

Electromagnetic field distribution inside the stack at the frequency of band-edge resonance is shown in Figs. 3 and 4 for the first two transmission resonances, respectively. For a given amplitude Ψ_I of the incident wave, the maximal field intensity $|\Psi(z)|^2$ inside the slab depends on the number N of the double layers in the stack and on the order number s of the resonance peak in Fig. 2

$$\max|\Psi(z)|^2 \propto |\Psi_I|^2 \left(\frac{N}{s}\right)^2. \tag{5}$$

The maximal field intensity (5) is proportional to the squared thickness of the slab and, for a large N, is greatly enhanced compared to that of the incident light. By contrast, at the slab boundaries at $z=0$ and $z=D=NL$, the field amplitude $\Psi(z)$ always remains comparable to Ψ_I to satisfy the electromagnetic boundary conditions (47). At frequencies outside the resonance transparency peaks, the field amplitude inside the stack drops sharply.

The exact definition of the physical values plotted in Figs. 3 and 4, as well as the numerical parameters of the periodic stacks used to generate these plots, are given in the Appendix.

The expressions (1)–(5) are valid if $N \gg 1$ and only apply to the transmission resonances close enough to the photonic band edge. In further consideration, we will focus on the most powerful first resonance $s=1$, closest to the photonic band edge.

Above, we outlined some basic features of the transmission band-edge resonance in finite stacks of isotropic layers. The question we would like to address in this paper is whether the presence of anisotropic layers in a finite periodic stack can qualitatively change the nature of the Fabry-Perot cavity resonance. We will show that, indeed, in periodic stacks involving anisotropic layers, the transmission resonance can be significantly stronger, compared to what is achievable with common periodic stacks of isotropic layers. For instance, in the periodic stack shown in Fig. 5, the field intensity associated with the transmission band-edge resonances can be proportional to N^4, rather than N^2. The latter implies that a stack of N anisotropic layers can perform as
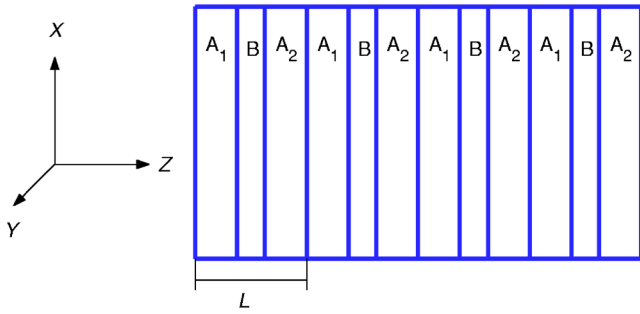
FIG. 5. (Color online) Periodic stack capable of supporting k-ω diagram with degenerate band edge. A unit cell L includes three layers: two birefringent layers A_1 and A_2 with different orientations φ_1 and φ_2 of the respective anisotropy axes in the X-Y plane, and one isotropic B layer. The misalignment angle $\varphi = \varphi_1 - \varphi_2$ between adjacent A layers must be different from 0 and $\pi/2$.

well as a common stack of N^2 isotropic layers. And this is a huge difference. The physical reason for this is that periodic stacks of anisotropic layers can support the kind of k-ω diagrams that are impossible in stacks of isotropic layers. Specifically, a dispersion curve $\omega(k)$ of the stack in Fig. 5 can develop a degenerate band edge, as shown in Fig. 6(b). Just below the degenerate band edge d, the dispersion curve can be approximated as

$$\omega \approx \omega_d + \frac{\omega_d''''}{24}(k - k_d)^4 \quad \text{where } \omega_d'''' = \left(\frac{\partial^4\omega}{\partial k^4}\right)_{k=k_d} < 0,$$
(6)

which implies a huge density of modes. And this is what makes all the difference compared to the case (2) of a regular band edge.

For convenience, the domain of definition of the Bloch wave number k in Fig. 6 is chosen between 0 and $2\pi/L$. Since the Bloch wave number is defined up to a multiple of $2\pi/L$, the representation in Fig. 6 is equivalent to that in Fig. 1(b). Note that the points a, g, and d in Figs. 6(a) and 6(b) lie at the Brillouin zone boundary at $k = \pi/L$.

In Fig. 7 we present the transmission dispersion of the finite periodic stacks in Fig. 5 composed of 32 unit cells L and having the k-ω diagram in Fig. 6(b). The frequency range shown includes the degenerate band edge (DBE) at $\omega = \omega_d$. The field intensity distribution at the frequency of the first transmission resonance 1 is shown in Fig. 8(b). One can see that for a given N, the resonant field intensity in Fig. 8 is significantly larger compared to that of the vicinity of a regular band edge, shown in Fig. 3. Specifically, in the case of a degenerate band edge

$$\max|\Psi(z)|^2 \propto |\Psi_I|^2 \left(\frac{N}{s}\right)^4,$$
(7)

compared to the estimation (5) related to a regular band edge. The transmission bandwidth in the case of the DBE appears to be much smaller.

In practice, the field amplitude associated with the transmission resonance is limited not only by the number of layers in the stack, but also by such factors as absorption, nonlinearity, imperfections of the periodic array, stack dimensions in the X-Y plane, incident radiation bandwidth, etc. All else being equal, the stack with degenerate band edge can have much fewer layers and, therefore can be much thinner compared to a regular stack of isotropic layers with similar performance. Much smaller dimensions can be very attractive for a variety of practical applications. On the
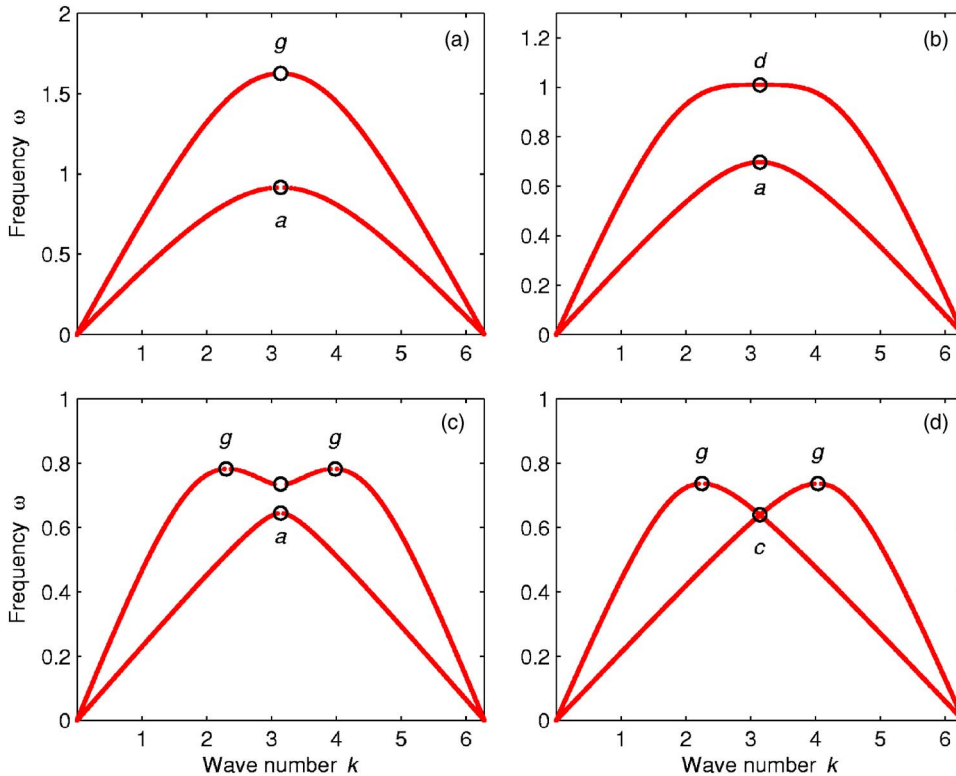

FIG. 6. (Color online) The first band of the k-ω diagram of the periodic stack in Fig. 5 for four different values of the B-layer thickness, D_B. (a) $D_B = 0.758\,91L$; this is the case of a regular band edge g. (b) $D_B = 0.458\,91L$; in this case the upper dispersion curve develops a degenerate band edge d. (c) $D_B = 0.358\,91L$; this is the case of a double band edge. (d) $D_B = 0$; in this case the two intersecting dispersion curves correspond to the pair of decoupled Bloch waves with different symmetries. The physical parameters of the periodic structure are specified in the Appendix .
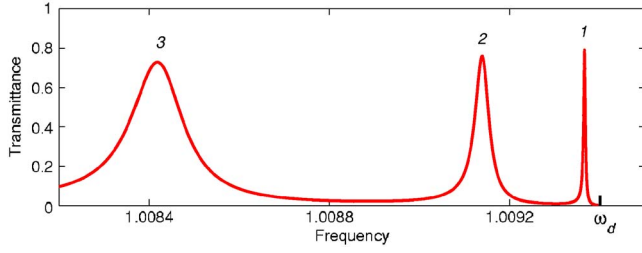
FIG. 7. (Color online) The transmission spectrum of periodic stack with the k-ω diagram in Fig. 6(b). The stack is composed of $N=32$ three-layered unit cells L in Fig. 5. The sharp transmission peaks below the degenerate band-edge frequency ω_d are associated with Fabry-Pérot cavity resonances.

downside, the realization of a k-ω diagram having a dispersion curve with a DBE requires more sophisticated periodic structures, such as the one shown in Fig. 5.

A similar effect can also be achieved in the waveguide environment, as well as in finite periodic arrays of coupled resonators. The essential requirement is the existence of degenerate band edge (6) on the k-ω diagram of the periodic array.

The rest of the paper is organized as follows.

In Sec. II we briefly outline the electrodynamics of periodic stratified media and examine the relation between anisotropy of the layers and the k-ω diagram of the stack. We show that at the frequency of degenerate band edge d, the 4×4 transfer matrix of a unit cell L cannot be diagonalized or even reduced to the block-diagonal form. Based on this, we establish necessary symmetry conditions for a periodic stack to develop a degenerate band edge (6) and to display the peculiar resonance properties associated with it. We prove that such periodic stacks must have at least two misaligned anisotropic layers in a unit cell, as shown in the example in Fig. 5.

In Sec. III, we consider the scattering problem for a finite periodic stack. We analyze the eigenmode composition of electromagnetic field at the frequency of transmission resonance near the degenerate band edge. We show that in contrast to the case (5) of a regular band edge, in the degenerate band-edge case (7) the resonance field inside the stack does not reduce to a superposition of forward and backward
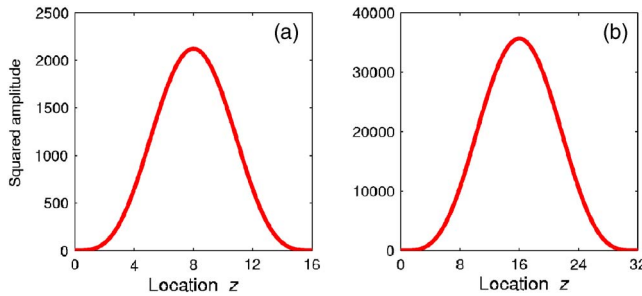

FIG. 8. (Color online) Smoothed intensity distribution inside periodic stack in Fig. 5 at the frequency of the first Fabry-Pérot resonance ($s=1$), closest to degenerate band edge d. The amplitude of the incident wave is unity. At the stack boundaries at $z=0$ and NL, the field intensity is of the order of unity, while inside the slab electromagnetic energy density is enhanced by a factor N^4. $N=$ (a) 16 and (b) 32.

propagating eigenmodes. Instead, the contribution of evanescent eigenmodes becomes equally important and leads to much stronger dependence (7) of the resonance field intensity on the number of layers in the stack.

The physical and geometrical parameters of stacks used for numerical simulations are specified in the Appendix.

II. ELECTRODYNAMICS OF PERIODIC STACKS OF ANISOTROPIC LAYERS

This section starts with a brief description of some basic electrodynamic properties of periodic layered media composed of lossless anisotropic layers. Then we turn to the particular case of periodic stacks with degenerate band edge. The scattering problem for periodic finite stacks, including the Fabry-Pérot cavity resonance in the vicinity of degenerate photonic band edge will be considered in the next section.

A. Transverse electromagnetic waves in stratified media

Our consideration is based on time-harmonic Maxwell equations in heterogeneous nonconducting media

$$\boldsymbol{\nabla} \times \vec{\mathbf{E}}(\vec{r}) = i\frac{\omega}{c}\vec{\mathbf{B}}(\vec{r}), \quad \boldsymbol{\nabla} \times \vec{\mathbf{H}}(\vec{r}) = -i\frac{\omega}{c}\vec{\mathbf{D}}(\vec{r}), \quad (8)$$

where the electric and magnetic fields and inductions are related by the linear constitutive equations

$$\vec{\mathbf{D}}(\vec{r}) = \hat{\varepsilon}(\vec{r})\vec{\mathbf{E}}(\vec{r}), \quad \vec{\mathbf{B}}(\vec{r}) = \hat{\mu}(\vec{r})\vec{\mathbf{H}}(\vec{r}). \quad (9)$$

In further consideration we assume the following.

(i) The direction of plane wave propagation coincides with the normal z to the layers.

(ii) The second-rank tensors $\hat{\varepsilon}(\vec{r})$ and $\hat{\mu}(\vec{r})$ are dependent on a single Cartesian coordinate z, normal to the layers.

(iii) The z direction is a twofold symmetry axis of the stack, implying that the anisotropy axes of individual layers are either parallel, or perpendicular to the z direction. The latter defines the case of in-plane anisotropy.

Under the above restrictions, the normal field components E_z and H_z of electromagnetic wave are zeros, and the system (8) of six time-harmonic Maxwell equations reduces to the following system of four ordinary linear differential equations for the transverse field components:

$$\frac{\partial}{\partial z}\Psi(z) = i\frac{\omega}{c}M(z)\Psi(z) \quad \text{where } \Psi(z) = \begin{bmatrix} E_x(z) \\ E_y(z) \\ H_x(z) \\ H_y(z) \end{bmatrix}. \quad (10)$$

The 4×4 matrix $M(z)$ in Eq. (10) is referred to as the (reduced) Maxwell operator.

In a lossless nonmagnetic medium with in-plane anisotropy, the electric permittivity and magnetic permeability tensors have the form

$$\hat{\varepsilon} = \begin{bmatrix} \varepsilon_{xx} & \varepsilon_{xy} & 0 \\ \varepsilon_{xy} & \varepsilon_{yy} & 0 \\ 0 & 0 & \varepsilon_{zz} \end{bmatrix}, \quad \hat{\mu} = \hat{1}. \tag{11}$$

This yields the following explicit expression for the Maxwell operator $M(z)$ in Eq. (10):

$$M(z) = \begin{bmatrix} 0 & 0 & 0 & 1 \\ 0 & 0 & -1 & 0 \\ -\varepsilon_{xy} & -\varepsilon_{yy} & 0 & 0 \\ \varepsilon_{xx} & \varepsilon_{xy} & 0 & 0 \end{bmatrix}, \tag{12}$$

where the components of the permittivity tensor may vary from layer to layer.

1. The transfer matrix formalism

The Cauchy problem

$$\frac{\partial}{\partial z}\Psi(z) = i\frac{\omega}{c}M(z)\Psi(z), \quad \Psi(z_0) = \Psi_0 \tag{13}$$

for the reduced Maxwell equation (10) has a unique solution

$$\Psi(z) = T(z,z_0)\Psi(z_0), \tag{14}$$

where the 4×4 matrix $T(z,z_0)$ is referred to as the *transfer matrix*. The transfer matrix (14) uniquely relates the values of time-harmonic electromagnetic field Ψ at any two points z and z_0 of the stratified medium. From the definition (14), it follows that

$$T(z,z_0) = T(z,z')T(z',z_0), \quad T(z,z_0) = T^{-1}(z_0,z), \quad T(z,z) = I. \tag{15}$$

The transfer matrix of a stack of layers is defined as

$$T_S = T(D,0),$$

where $z=0$ and D are the stack boundaries. The greatest advantage of the transfer matrix formalism stems from the fact that the transfer matrix of an arbitrary stack is a sequential product of the transfer matrices T_m of the constitutive layers

$$T_S = \prod_m T_m. \tag{16}$$

If the individual layers m are homogeneous, the corresponding single-layer transfer matrices T_m can be explicitly expressed in terms of the respective Maxwell operators M_m

$$T_m = \exp(iD_m M_m), \tag{17}$$

where D_m is the thickness of the mth layer. The explicit expression for the Maxwell operator M_m of a uniform dielectric layer with in-plane anisotropy is given by Eq. (12). Thus, Eq. (16) together with Eqs. (12) and (17) provide an explicit analytical expression for the transfer matrix T_S of a stack of dielectric layers with in-plane anisotropy.

The 4×4 transfer matrix of an arbitrary lossless stratified medium displays the fundamental property of J unitarity [15]

$$T^\dagger = JT^{-1}J \quad \text{where } J = \begin{bmatrix} 0 & 0 & 0 & 1 \\ 0 & 0 & -1 & 0 \\ 0 & -1 & 0 & 0 \\ 1 & 0 & 0 & 0 \end{bmatrix}, \tag{18}$$

which implies, in particular, that

$$|\det T| = 1. \tag{19}$$

Different versions of the 4×4 transfer matrix formalism have been used in electrodynamics of stratified media composed of birefringent and/or gyrotropic layers for decades (see, for example, [10–12] and references therein). In this paper we use exactly the same notations and terminology as in our previous publications [13–16] on electrodynamics of stratified media.

B. Eigenmodes in periodic layered media

In a periodic layered medium, all material tensors are periodic functions of z, and so is the 4×4 matrix $M(z)$ in Eq. (10). Usually, the solutions $\Psi_k(z)$ of the reduced Maxwell equation (10) with the periodic $M(z)$ can be chosen in the Bloch form

$$\Psi_k(z + L) = e^{ikL}\Psi_k(z), \tag{20}$$

where the Bloch wave number k is defined up to a multiple of $2\pi/L$. The definition (14) of the transfer matrix together with Eq. (20) yields

$$T(z + L,z)\Psi_k(z) = e^{ikL}\Psi_k(z). \tag{21}$$

Introducing the transfer matrix of a unit cell L

$$T_L = T(L,0), \tag{22}$$

we have from Eq. (21)

$$T_L\Phi_k = e^{ikL}\Phi_k \quad \text{where } \Phi_k = \Psi_k(0). \tag{23}$$

Thus, the eigenvectors of the transfer matrix T_L of the unit cell are uniquely related to the Bloch solutions $\Psi_k(z)$ of the reduced Maxwell equation (10),

$$\Phi_i = \Psi_i(0), \quad i = 1,2,3,4. \tag{24}$$

The corresponding four eigenvalues

$$X_i = e^{ik_iL}, \quad i = 1,2,3,4, \tag{25}$$

of T_L are the roots of the characteristic polynomial $F_4(X)$ of the fourth degree

$$F_4(X) = \det(T_L - XI) = 0. \tag{26}$$

The unit cell of a periodic stack can be chosen differently. For example, the choice A_1-B-A_2 specified in Fig. 5 is as good as A_2-A_1-B. A different choice of a unit cell corresponds to its shift in the z direction and results in the following transformation of the corresponding transfer matrix T_L:

$$T_L' = T(0,Z)T_L T(Z,0) = [T(Z,0)]^{-1}T_L T(Z,0), \tag{27}$$

where Z is the amount of the shift. The modified transfer matrix is similar to the original one and has the same set of eigenvalues.

For any given ω, the characteristic equation (26) defines a set of four eigenvalues (25). Real k (or, equivalently, $|X|=1$) correspond to propagating Bloch modes, while complex k (or, equivalently, $|X| \neq 1$) correspond to evanescent modes.

The J unitarity (18) of T_L imposes the following restriction on its eigenvalues (25):

$$\{X_i^{-1}\} \equiv \{X_i^*\}, \quad i=1,2,3,4, \qquad (28)$$

or, equivalently,

$$\{k_i\} \equiv \{k_i^*\}, \quad i=1,2,3,4, \qquad (29)$$

for any given ω. In view of the relations (28) and (29), one can distinguish the following three different situations.

(A) All four wave numbers are real,

$$k_1 \equiv k_1^*, \quad k_2 \equiv k_2^*, \quad k_3 \equiv k_3^*, \quad k_4 \equiv k_4^*. \qquad (30)$$

In the example in Fig. 6, this case relates to the frequency range

$$0 < \omega < \omega_a. \qquad (31)$$

In this case, all four Bloch eigenmodes are propagating.

(B) Two wave numbers are real and the other two are complex,

$$k_1 = k_1^*, \quad k_2 = k_2^*, \quad k_4 = k_3^* \quad \text{where } k_3 \neq k_3^*, \quad k_4 \neq k_4^*. \qquad (32)$$

This case relates to the frequency range

$$\omega_a < \omega < \omega_g \qquad (33)$$

in Fig. 6(a), or the frequency range

$$\omega_a < \omega < \omega_d \qquad (34)$$

in Fig. 6(b). In both cases (33) and (34), two of the four Bloch eigenmodes are propagating and the remaining two are evanescent with complex conjugated wave numbers.

(C) All four wave numbers are complex,

$$k_2 = k_1^*, \quad k_4 = k_3^* \quad \text{where } k_1 \neq k_1^*, \quad k_2 \neq k_2^*, \quad k_3 \neq k_3^*,$$

$$k_4 \neq k_4^*. \qquad (35)$$

This situation relates to a frequency gap, where all four Bloch eigenmodes are evanescent. In the example in Fig. 6, this case corresponds to

$$\omega_g < \omega \quad \text{or} \quad \omega_d < \omega. \qquad (36)$$

Notice that the case B of two propagating and two evanescent modes can only occur in periodic stacks of anisotropic layers. If all the layers in a unit cell are isotropic, the four Bloch eigenmodes are either all propagating or all evanescent, as is the case in Fig. 1. For a given frequency ω, the four Bloch eigenmodes correspond to two different polarizations and two opposite directions of propagation.

1. Non-Bloch solutions at stationary points of the k-ω diagram

So far, we have considered only the cases where all four solutions for the reduced Maxwell equation (10) can be cho-sen in the Bloch form (20). All such cases fall into one of the following three categories: (A) all four eigenmodes are propagating, (B) two modes are propagating and the other two are evanescent, (C) all four eigenmodes are evanescent. This classification of the eigenmodes does not apply at the frequencies of stationary points on the k-ω diagram, where the group velocity u of some of the propagating modes vanishes,

$$u = d\omega/dk = 0. \qquad (37)$$

At a stationary point of a dispersion curve, not all four solutions of the Maxwell equation (10) are Bloch waves, as defined in (20). Instead, some of the solutions can be algebraically diverging non-Bloch eigenmodes. Such eigenmodes can be essential for understanding the resonance effects in finite and semi-infinite periodic arrays.

Let us consider the situation at stationary points (37) on the k-ω diagram in terms of the matrix T_L. Although at any given frequency ω, the reduced Maxwell equation (10) has exactly four linearly independent solutions, it does not imply that the respective transfer matrix T_L in (23) must have four linearly independent eigenvectors (23). Indeed, although the matrix T_L is invertible, it is neither Hermitian, nor unitary and, therefore, may not be diagonalizable. Specifically, if the frequency approaches one of the stationary points (37), some of the eigenvectors Φ_k in (23) become nearly parallel to each other. Eventually, as ω reaches the stationary point value, the number of linearly independent eigenvectors Φ_k becomes less than four, and the relation (24) does not apply at that point.

Examples of different stationary points (37) are shown in Fig. 6. Using these examples, let us take a closer look at these special frequencies.

At the frequencies ω_g of the photonic band edge g in Fig. 6(a), the four eigenmodes include one propagating mode with $k=\pi/L$ and zero group velocity; one non-Bloch eigenmode linearly diverging with z; and a pair of evanescent modes with equal and opposite imaginary wave numbers.

At the frequencies ω_a corresponding to the point a in Fig. 6, the four solutions of Eq. (10) include the propagating mode with $k=\pi/L$ and zero group velocity; one non-Bloch eigenmode linearly diverging with z; and a pair of propagating modes having equal and opposite group velocities and belonging to the dispersion curve other than the one containing the point a.

Of special interest here is the frequency ω_d of the degenerate photonic band edge d in Fig. 6(b). In this case, the four solutions of Eq. (10) include [17] the propagating mode with $k=\pi/L$ and zero group velocity, and three non-Bloch eigenmodes diverging as z, z^2, and z^3, respectively.

At any particular frequency, the existence of non-Bloch eigenmodes can be directly linked to the canonical Jordan form of the corresponding transfer matrix T_L. Indeed, the 4×4 matrix T_L, being invertible, can have one of the following five different canonical forms

$$\tilde{T}_1 = \begin{bmatrix} X_1 & 0 & 0 & 0 \\ 0 & X_2 & 0 & 0 \\ 0 & 0 & X_3 & 0 \\ 0 & 0 & 0 & X_4 \end{bmatrix},$$

$$\tilde{T}_{21} = \begin{bmatrix} X_1 & 1 & 0 & 0 \\ 0 & X_1 & 0 & 0 \\ 0 & 0 & X_3 & 0 \\ 0 & 0 & 0 & X_4 \end{bmatrix}, \quad \tilde{T}_{22} = \begin{bmatrix} X_1 & 1 & 0 & 0 \\ 0 & X_1 & 0 & 0 \\ 0 & 0 & X_2 & 1 \\ 0 & 0 & 0 & X_2 \end{bmatrix},$$

$$\tilde{T}_3 = \begin{bmatrix} X_1 & 1 & 0 & 0 \\ 0 & X_1 & 1 & 0 \\ 0 & 0 & X_1 & 0 \\ 0 & 0 & 0 & X_2 \end{bmatrix}, \quad \tilde{T}_4 = \begin{bmatrix} X & 1 & 0 & 0 \\ 0 & X & 1 & 0 \\ 0 & 0 & X & 1 \\ 0 & 0 & 0 & X \end{bmatrix}, \quad (38)$$

of which all but $\tilde{T}_1$ have nontrivial Jordan blocks and, therefore, are not diagonalizable. Each $m \times m$ Jordan block is associated with a single eigenvector of the corresponding T matrix. Therefore, the total number of eigenvectors of the different 4×4 matrices in (38) is less than the number 4 of the solutions for the reduced Maxwell equation (10). The only exception is the diagonalizable case $\tilde{T}_1$, where the four T_L eigenvectors correspond to four Bloch eigenmodes, as prescribed by (24). Generally, each nontrivial $m \times m$ Jordan block of the T matrix is associated with the m eigenmodes of Eq. (10), of which one is a propagating Bloch eigenmode with zero group velocity, and the other $m-1$ are non-Bloch eigenmodes algebraically diverging with z. The details can be found in any course on linear algebra, for example, [18–21]. Let us consider each case separately.

At general frequencies, different from those of stationary points (37), the 4×4 matrix T_L is always diagonalizable. Its canonical (diagonalized) form is trivial and coincides with $\tilde{T}_1$ in (38). The four eigenvectors are defined in (24). All the possibilities here reduce to one of the three cases A, B, or C described earlier in this section. None of them involves non-Bloch solutions.

At the frequency ω_g of a regular photonic band edge in Fig. 6(a), the canonical Jordan form of the respective transfer matrix is $\tilde{T}_{21}$ in (38), where

$$X_1 = -1, \quad X_3 = X_3^* = X_4^{-1} \neq 1.$$

The 2×2 Jordan block relates to one propagating Bloch mode with $k = \pi/L$ and zero group velocity, and one non-Bloch linearly diverging eigenmode. The pair of real eigenvalues X_3 and $X_4 = X_3^{-1}$ relate to the pair of evanescent modes at $\omega = \omega_g$.

By contrast, at the frequency of photonic band edge g in Fig. 1(b) related to the stack of isotropic layers, there are no evanescent modes. The canonical Jordan form of the corresponding transfer matrix coincides with $\tilde{T}_{22}$ in (38), where

$$X_1 = X_2 = -1.$$

Each of the two 2×2 identical Jordan blocks relates to one propagating Bloch mode with $k = \pi/L$ and zero group velocity, as well as one non-Bloch linearly diverging eigenmode. The two Jordan blocks of $\tilde{T}_{22}$ correspond to two different polarizations of light.

At the frequency ω_a in Fig. 6, the canonical Jordan form of the respective transfer matrix is $\tilde{T}_{21}$, where

$$X_1 = -1, \quad X_3 = X_4^*, \quad |X_3| = |X_4| = 1.$$

The double eigenvalue $X_1 = -1$ of the 2×2 Jordan block relates to one propagating Bloch mode with $k = \pi/L$ and zero group velocity, and one non-Bloch linearly diverging eigenmode. The pair of complex eigenvalues X_3 and $X_4 = X_3^*$ relate to the pair of propagating modes having equal and opposite group velocities and belonging to the dispersion curve other than the one containing the point a.

The canonical form $\tilde{T}_3$ in (38) relates to a k-ω diagram with stationary inflection point. Such a stationary point cannot be realized in a reciprocal periodic stack at normal light propagation [14,15].

Of particular interest here is the case (6) of a degenerate band edge. At the degenerate band-edge frequency ω_d, the canonical Jordan form of the transfer matrix is $\tilde{T}_4$ in (38),

$$T_L \sim \tilde{T}_4 = \begin{bmatrix} X & 1 & 0 & 0 \\ 0 & X & 1 & 0 \\ 0 & 0 & X & 1 \\ 0 & 0 & 0 & X \end{bmatrix} \quad \text{where } X = \pm 1. \quad (39)$$

More specifically, in the case shown in Fig. 6(b),

$$X = X_d = e^{ik_dL} = -1 \quad \text{at } \omega = \omega_d.$$

The matrix (39) presents a single 4×4 Jordan block and has a single eigenvector, corresponding to the propagating eigenmode with $k = \pi/L$ and zero group velocity. The other three solutions for the Maxwell equation (10) at $\omega = \omega_d$ are non-Bloch eigenmodes diverging as z, z^2, and z^3, respectively.

If the frequency ω deviates from the stationary point (37), the transfer matrix T_L becomes diagonalizable with the canonical Jordan form $\tilde{T}_1$ in (38). The perturbation theory relating the non-Bloch eigenmodes at the frequency of the degenerate band edge to the Bloch eigenmodes in the vicinity of this point is presented in [17].

C. Symmetry conditions for the existence of a degenerate band edge

Not all periodic stacks can develop a degenerate band edge, defined in Eq. (6). Some fundamental restrictions can be derived from symmetry considerations. These restrictions stem from the fact that at the frequency ω_d of the degenerate band edge, the transfer matrix T_L must have the Jordan canonical form (39). Such a matrix cannot be reduced to a block-diagonal form, let alone diagonalized. Therefore, a necessary condition for the existence of degenerate band edge is that the symmetry of the periodic array does not impose the reducibility of the transfer matrix T_L to a block-diagonal form.

The above condition does not imply that the transfer matrix T_L must not be reducible to a block-diagonal form at *any* frequency ω on the k-ω diagram. Indeed, at a general frequency ω, the matrix T_L is certainly reducible, and even diagonalizable. The strength of *the symmetry-imposed* reducibility is that it leaves no room for exceptions, such as the frequency ω_d of degenerate band edge, where the transfer matrix T_L must not be reducible to a block-diagonal form.

Therefore, in the case of symmetry-imposed reducibility, the very existence of a degenerate band edge is ruled out. Observe that in most periodic layered structures, the symmetry of the periodic array *does require* the matrix T_L to be similar to a block-diagonal matrix at all frequencies. In all these cases, the stack symmetry is incompatible with the existence of degenerate band edge on the k-ω diagram.

Let us apply the above criterion to some specific cases.

In periodic stacks of isotropic layers, the Maxwell equations for the waves with the x and y polarizations are identical and decoupled, implying that the respective transfer matrix can be reduced to the block-diagonal form

$$\widetilde{T}_L = \begin{bmatrix} T_{11} & T_{12} & 0 & 0 \\ T_{21} & T_{22} & 0 & 0 \\ 0 & 0 & T_{11} & T_{12} \\ 0 & 0 & T_{21} & T_{22} \end{bmatrix}. \tag{40}$$

The two identical blocks in (40) correspond to two different polarizations of light. The characteristic polynomial $F_4(X)$ of the block-diagonal matrix (40) factorizes into a product of two identical second-degree polynomials related to electromagnetic waves with the x and y polarizations, respectively,

$$F_4(X) = F_2(X)F_2(X). \tag{41}$$

The block-diagonal structure of the matrix (40) rules out the existence of a degenerate band edge in periodic stacks of isotropic layers. In fact, the transfer matrix T_L in this case can only have the following two canonical forms:

$$\widetilde{T}_1 = \begin{bmatrix} X & 0 & 0 & 0 \\ 0 & X^{-1} & 0 & 0 \\ 0 & 0 & X & 0 \\ 0 & 0 & 0 & X^{-1} \end{bmatrix}, \quad \widetilde{T}_{22} = \begin{bmatrix} \pm 1 & 1 & 0 & 0 \\ 0 & \pm 1 & 0 & 0 \\ 0 & 0 & \pm 1 & 1 \\ 0 & 0 & 0 & \pm 1 \end{bmatrix},$$

compatible with (40). The case $\widetilde{T}_1$ relates to a general frequency, while the case $\widetilde{T}_{22}$ relates to a photonic band edge, like the one shown in Fig. 1(b).

Let us now turn to the situation where all or some of the layers of the periodic stack are birefringent. The in-plane dielectric anisotropy (11) may allow for a degenerate band edge on the k-ω diagram, but not automatically.

Let us start with the simplest periodic array in which all anisotropic layers of the stack have aligned in-plane anisotropy. The term "aligned" means that one can choose the directions of the in-plane Cartesian axes x and y so that the permittivity tensors in all layers are diagonalized simultaneously. In this setting, the Maxwell equations for the waves with the x and y polarizations are still separated, implying that the respective transfer matrix can be reduced to the block-diagonal form,

$$\widetilde{T}_L = \begin{bmatrix} T_{11} & T_{12} & 0 & 0 \\ T_{21} & T_{22} & 0 & 0 \\ 0 & 0 & T_{33} & T_{34} \\ 0 & 0 & T_{43} & T_{44} \end{bmatrix}. \tag{42}$$

The two blocks in (42) correspond to the x and y polarizations of light. The fourth degree characteristic polynomial of the block-diagonal matrix (42) factorizes into the product

$$F_4(X) = F_x(X)F_y(X), \tag{43}$$

where $F_x(X)$ and $F_y(X)$ are independent second-degree polynomials related to electromagnetic waves with the x and y polarizations, respectively. The typical k-ω diagram in this case will be similar to that shown in Fig. 6(a) with two separate curves related to two linear polarizations of light. Again, the block-diagonal structure of the matrix (42) rules out the existence of a degenerate band edge in periodic stacks with aligned anisotropic layers. The transfer matrix T_L in this case can only have the following two canonical forms:

$$\widetilde{T}_1 = \begin{bmatrix} X_1 & 0 & 0 & 0 \\ 0 & X_1^{-1} & 0 & 0 \\ 0 & 0 & X_2 & 0 \\ 0 & 0 & 0 & X_2^{-1} \end{bmatrix}, \quad \widetilde{T}_{22} = \begin{bmatrix} \pm 1 & 1 & 0 & 0 \\ 0 & \pm 1 & 0 & 0 \\ 0 & 0 & X & 0 \\ 0 & 0 & 0 & X^{-1} \end{bmatrix},$$

compatible with (42). The case $\widetilde{T}_1$ relates to a general frequency, while the case $\widetilde{T}_{22}$ relates to a photonic band edge.

As we have seen, the presence of anisotropic layers may not necessarily lift the symmetry prohibition for the degenerate band edge, because the symmetry of the periodic array may still be incompatible with the canonical Jordan form (39). Generally if the space symmetry group G of the layered structure includes a mirror plane $m_\parallel$ parallel to the z direction, this would guarantee the reducibility of the matrix T_L to a block-diagonal form. Indeed, a standard line of reasoning gives that if $m_\parallel \in G$, and the y axis is chosen perpendicular to the mirror plane $m_\parallel$, then the waves with the x and y polarizations have different parity with respect to the symmetry operation of reflection and, therefore, are decoupled. The latter leads to reducibility of the matrix T_L to the block-diagonal form (42). Thus, a formal necessary condition for the existence of a degenerate band edge on the k-ω diagram can be written as follows:

$$m_\parallel \notin G. \tag{44}$$

None of the common periodic layered structures satisfy this criterion and, therefore, none of them can develop the degenerate band edge. For example, even if anisotropic layers are present, but the anisotropy axes in all anisotropic layers are either aligned or perpendicular to each other, the symmetry group G of the stack still has the mirror plane $m_\parallel$, which guarantees the separation of the x and y polarizations and the reducibility of the corresponding transfer matrix T_L to the block-diagonal form (42). The only way to satisfy the condition (44), and thereby to allow for the degenerate band edge on the k-ω diagram, is to have at least two misaligned

anisotropic layers in a unit cell with the misalignment angle being different from 0 and $\pi/2$, as shown in the example in Fig. 5.

Observe that the presence of B layers in the periodic array in Fig. 5 is also essential, unless the two anisotropic layers A_1 and A_2 have different thicknesses or are made of different anisotropic materials. In Fig. 5, the layers A_1 and A_2 differ only by their orientation in the x-y plane, but otherwise they are identical. In such a case, if the B layers are removed, the point symmetry group of the periodic stack in Fig. 5 rises from D_2 to D_{2h}, acquiring the glide mirror plane $m_\parallel$. This, according to the criterion (44), imposes the reducibility of the matrix T_L to the block-diagonal form (42), regardless of the misalignment angle between the adjacent A layers. The symmetry-imposed reducibility rules out the possibility of the degenerate band edge (6). The k-ω diagram of the periodic stack in Fig. 5 with the B layers removed is shown in Fig. 6(d).

In the numerical example considered in the next section, the B layers are simply empty gaps of certain thickness D_B between the adjacent double layers A_1-A_2. The misalignment angle is chosen $\pi/4$. By changing the thickness D_B of the gap B, one can change the k-ω diagram of the periodic stack, as shown in Fig. 6. A similar effect can be achieved by changing the misalignment angle between the adjacent A layers.

III. TRANSMISSION RESONANCE IN THE VICINITY OF THE DEGENERATE BAND EDGE

A. Scattering problem for periodic semi-infinite stack

To solve the scattering problem for a plane monochromatic wave incident on a finite stack of anisotropic layers we use the following standard approach based on the 4×4 transfer matrix.

Let $\Psi_I(z)$, $\Psi_R(z)$, and $\Psi_P(z)$ be the incident, reflected, and passed plane waves in vacuum. Allowing for general elliptic polarization of the waves, we have

$$\Psi_I(z) = \begin{bmatrix} A_x \\ A_y \\ -A_y \\ A_x \end{bmatrix} e^{i(\omega/c)z}, \quad \Psi_R(z) = \begin{bmatrix} R_x \\ R_y \\ R_y \\ -R_x \end{bmatrix} e^{-i(\omega/c)z},$$

$$\Psi_P(z) = \begin{bmatrix} P_x \\ P_y \\ -P_y \\ P_x \end{bmatrix} e^{i(\omega/c)z}.$$

The domains of definition are

$$z \leq 0 \quad \text{for } \Psi_I(z) \text{and } \Psi_R(z),$$

$$D \leq z \quad \text{for } \Psi_P(z), \tag{45}$$

where D is the stack thickness. The field inside the stack is denoted by $\Psi_T(z)$. Except for the stationary points (37) on the k-ω diagram, $\Psi_T(z)$ can be decomposed into a superpo-

sition of the four Bloch solutions (20) of the Maxwell equation (10)

$$\Psi_T(z) = \sum_k \Psi_k(z), \quad 0 \leq z \leq D. \tag{46}$$

This representation is meaningful if the periodic stack contains a significant number of unit cells L. Otherwise, if there are just a few layers in the stack, the representation (46) is formally valid, but not particularly useful.

The boundary conditions at the two slab/vacuum interfaces are

$$\Psi_T(0) = \Psi_I(0) + \Psi_R(0), \quad \Psi_T(D) = \Psi_P(D). \tag{47}$$

The transfer matrix T_S of a periodic stack is

$$T_S = (T_L)^N. \tag{48}$$

The relation

$$\Psi(D) = T_S\Psi(0), \tag{49}$$

together with the pair of boundary conditions (47), allows us to express both the reflected wave Ψ_R and the wave Ψ_P passed through the slab, in terms of a given incident wave Ψ_I and the elements of the transfer matrix T_S. This also gives the transmittance and reflectance coefficients of the slab defined as

$$\tau_D = \frac{S_P}{S_I} = \frac{|\Psi_P(D)|^2}{|\Psi_I(0)|^2}, \quad \rho_D = -\frac{S_R}{S_I} = \frac{|\Psi_R(0)|^2}{|\Psi_I(0)|^2}, \tag{50}$$

where $S = cW$ is the Poynting vector of the corresponding wave. In the case of a lossless stack

$$\tau_D + \rho_D = 1.$$

The field distribution $\Psi_T(z)$ inside the slab is found using either of the following expressions

$$\Psi_T(z) = T(z,0)[\Psi_I(0) + \Psi_R(0)] = T(z,D)\Psi_P(D),$$

$$0 \leq z \leq D. \tag{51}$$

The above procedure is commonly used for the frequency-domain analysis of periodic and nonperiodic layered structures involving anisotropic and/or gyrotropic layers.

In addition to the field distribution inside the slab, we are also interested in its eigenmode composition. The latter is particularly important since it allows us to explain the fundamental difference between Fabry-Pérot resonance in the vicinity of a degenerate band edge and a similar resonance in the vicinity of a regular band edge. Throughout this section we consider only the first transmission resonance, closest to the band edge.

B. Field composition at the frequency of transmission resonance

In the case of transmission resonance in a periodic stack of isotropic layers, the resonance field inside the stack is a simple standing wave composed of two propagating Bloch
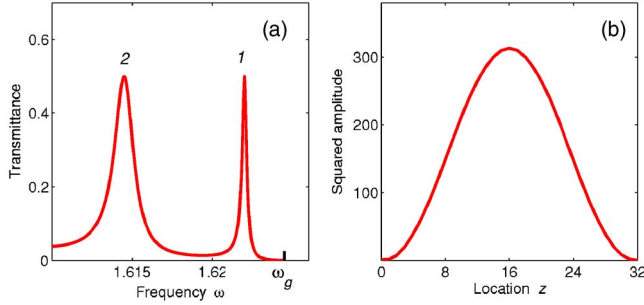
FIG. 9. (Color online) Transmission resonance in the vicinity of regular photonic band edge g in Fig. 6(a) in the stack composed of 32 unit cells L. (a) Transmission dispersion at the frequency range including the regular BE g and two closest transmission resonances. (b) Smoothed field intensity distribution (A3) inside the stack at the frequency ω_1 of the first transmission resonance 1.

modes with opposite group velocity [see Eqs. (1)–(5) and the discussion of them]. The introduction of anisotropy in itself does not change qualitatively the resonance picture, as shown in Fig. 9. The only difference is that the electromagnetic field $\Psi_T(z)$ inside the stack can now have both propagating and evanescent components. But at the frequency of a transmission resonance, the contribution of the evanescent components is negligible, as shown in Fig. 10. So, basically, one can still see the resonance field inside the stack as a simple standing wave composed of a pair of propagating modes with greatly enhanced amplitude, compared to that of the incident wave. The formulas (1)–(5) still apply here, provided that the number N of unit cells in the stack is not too small.

In Fig. 10(a) we show the squared amplitudes (intensity distributions)

$$|\Psi_j(z)|^2, \quad j = 1,2,3,4, \tag{52}$$

of the individual Bloch components of the resulting field $\Psi_T(z)$ at the frequency of the first transmission resonance near the regular band edge g in Fig. 6(a). The numbers 1 and 2 designate the forward and backward propagating components of the standing wave. The evanescent contributions 3
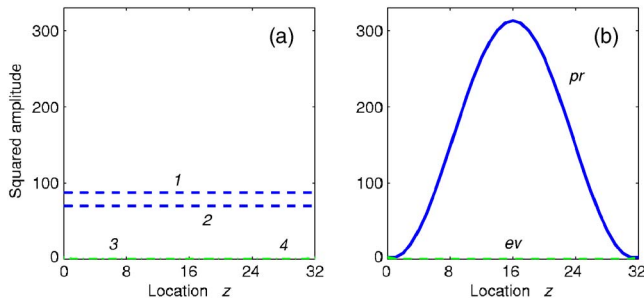

FIG. 10. (Color online) The Bloch composition of the resonant field in Fig. 9(b) corresponding to the transmission peak 1 in Fig. 9(a). (a) Square moduli of each of the four Bloch components; 1 and 2 are forward and backward propagating components; 3 and 4 are the evanescent components, which are negligible. (b) Square moduli of the combined contribution of two propagating components (pr), and the combined contribution of two evanescent components (ev). The evanescent modes' contribution is negligible.

and 4 are negligible. In Fig. 10(b) we show the squared amplitudes of the combined contribution of the pair of propagating waves (pr), and the combined contribution of the pair of evanescent waves (ev)

$$|\Psi_{pr}(z)|^2 = |\Psi_1(z) + \Psi_2(z)|^2, \quad |\Psi_{ev}(z)|^2 = |\Psi_3(z) + \Psi_4(z)|^2. \tag{53}$$

Obviously,

$$\Psi_T(z) \approx \Psi_{pr}(z). \tag{54}$$

Now let us turn to the case of transmission resonance in the vicinity of degenerate band edge d in Fig. 6(b). There are several features that sharply distinguish this case from the similar transmission resonance near the regular band edge g in Fig. 6(a).

First of all, for a given number N of unit cells in the stack ($N=32$), the field intensity in Fig. 8(b) is by several orders of magnitude higher, compared to that in Fig. 9(b), in spite of the close similarity of all numerical parameters of the respective periodic structures (see the Appendix). In the case of transmission resonance in the vicinity of the degenerate band edge, the resonance field intensity increases as N^4, while in the case of a regular band edge, the field intensity is proportional to N^2.

The second distinction is that in the case of degenerate band edge, the field intensity near the slab boundaries at $z=0$ and $z=D$, increases as

$$|\Psi_T(z)|^2 \propto z^4, \quad (D-z)^4, \quad \text{DBE case.} \tag{55}$$

By contrast, in the case of a regular band edge, the field intensity near the stack boundaries rises at a much slower rate

$$|\Psi_T(z)|^2 \propto z^2, \quad (D-z)^2, \quad \text{regular BE case,} \tag{56}$$

which is characteristic of a regular standing wave composed of two propagating components.

Finally, in the case of a regular band edge, the transmission resonance field $\Psi_T(z)$ is a standing wave composed of two propagating Bloch modes with opposite group velocities. The evanescent modes do not participate in the formation of the resonance field, as clearly seen in Fig. 10. By contrast, in the case of transmission resonance in the vicinity of the DBE, the role of evanescent components in the formation of the resonance field is absolutely crucial. Indeed, as shown in Fig. 11, amplitudes of the propagating and evanescent components are comparable in magnitude. More importantly, the combined contribution $\Psi_{pr}(z)$ of the two propagating components does not even resemble a standing wave with the nodes at the slab boundary, as was the case in Fig. 10(b). Instead, comparing Figs. 8(b) and 11(b) we see that at the slab boundaries at $z=0$ and D, the propagating and evanescent components interfere destructively, almost canceling each other,

$$\Psi_{pr}(z) \approx -\Psi_{ev}(z) \quad \text{at } z = 0 \text{ and } z = D,$$

while the individual Bloch components (52) remain huge. We recall that in all cases the intensity of the incident wave Ψ_I is unity.
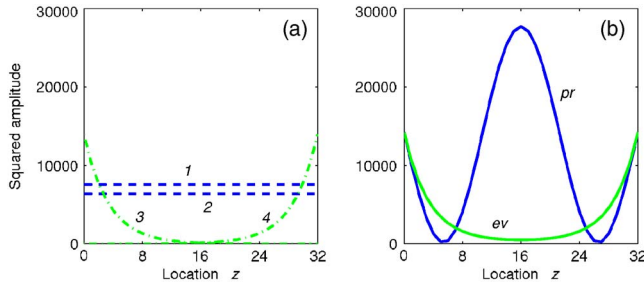
FIG. 11. (Color online) The Bloch composition of the resonant field in Fig. 8(b) corresponding to the transmission peak 1 in Fig. 7. (a) Square moduli of each of the four Bloch components, 1 and 2 are forward and backward propagating components. (b) Square moduli of the combined contribution of two propagating components (*pr*), and the combined contribution of two evanescent components (*ev*). Propagating and evanescent contributions interfere destructively at the slab boundaries.

Qualitatively, such a bizarre resonance behavior in the vicinity of the degenerate band edge can be characterized as follows. As we already mentioned, at the frequency ω_d of degenerate band edge, three of the four solutions for the Maxwell equation (10) are non-Bloch eigenmodes diverging as z, z^2, z^3. Although the frequency ω_1 of the transmission cavity resonance is slightly different from ω_d and, therefore, all four eigenmodes are Bloch waves, the close proximity of ω_1 to ω_d causes all the abnormalities seen in Fig. 11. To describe this behavior in a mathematically consistent way, one should start with the set of the Bloch and non-Bloch solutions at $\omega = \omega_d$ as zero approximation. Then, using the perturbation theory for the nondiagonalizable transfer matrix $T_L(\omega_d)$, one can derive an asymptotic theory for the case of large N. The perturbation theory for the degenerate band edge d was developed in [17]. It turns out that near the slab boundaries at $z \ll D$ and $(D-z) \ll D$, the field $\Psi_T(z)$ at the transmission resonance frequency ω_1 is well approximated by a quadratically diverging non-Bloch eigenmode, corresponding to $\omega = \omega_d$. It qualitatively explains the extremely rapid growth (55) of the resonance field inside the slab as one moves away from either slab boundary. It also explains the sharp dependence (7) of the resonance field intensity on the number N of unit cells in the stack.

ACKNOWLEDGMENTS

APPENDIX

1. Numerical parameters of layered arrays

The periodic array in Fig. 5 has three layers in a unit cell L, of which two (A_1 and A_2) are anisotropic and have the same thickness D_A. The third layer B is isotropic with the thickness D_B. In our numerical simulations, the B layers are empty gaps of variable thickness.

The anisotropic layers A_1 and A_2 are made of the same lossless dielectric material and have the same thickness. The corresponding dielectric permittivity tensor is

$$\hat{\varepsilon} = \begin{bmatrix} \varepsilon_A + \delta\cos 2\varphi & \delta\sin 2\varphi & 0 \\ \delta\sin 2\varphi & \varepsilon_A - \delta\cos 2\varphi & 0 \\ 0 & 0 & \varepsilon_{zz} \end{bmatrix},$$

where δ describes the magnitude of in-plane anisotropy, while the angle φ defines the orientation of the anisotropy axes of the corresponding layer in the x-y plane. The most critical parameter of the periodic structure in Fig. 5 is the misalignment angle

$$\varphi = \varphi_1 - \varphi_2 \tag{A1}$$

between the adjacent anisotropic layers A_1 and A_2. This angle determines the symmetry of the periodic array and, eventually, what kind of k-ω diagram it can display. It is important for our purposes that the misalignment angle is different from 0 and $\pi/2$. In our numerical simulations we set

$$\varphi_1 = 0, \quad \varphi_2 = \pi/4,$$

and use the following expressions for the dielectric permittivity of the A layers:

$$\hat{\varepsilon}_{A1} = \begin{bmatrix} \varepsilon_A + \delta & 0 & 0 \\ 0 & \varepsilon_A - \delta & 0 \\ 0 & 0 & \varepsilon_{zz} \end{bmatrix}, \quad \hat{\varepsilon}_{A2} = \begin{bmatrix} \varepsilon_A & \delta & 0 \\ \delta & \varepsilon_A & 0 \\ 0 & 0 & \varepsilon_{zz} \end{bmatrix}. \tag{A2}$$

In our numerical simulations we set

$$\varepsilon_A = 13.61, \quad \delta = 12.4.$$

The numerical value of ε_{zz} is irrelevant.

In the case of the periodic array of isotropic layers in Fig. 1(a), we set

$$\varepsilon_A = 3.78, \quad \delta = 0, \quad D_A = D_B = 0.5L.$$

2. Description of plots

In all plots of the transmission dispersion and field intensity distribution, the incident wave is linearly polarized parallel to the Y axis.

In all plots of the field intensity distribution we, in fact, plotted the following physical quantity:

$$\langle|\Psi(z)|^2\rangle = \langle \vec{E}(z) \cdot \vec{E}^*(z) + \vec{H}(z) \cdot \vec{H}^*(z)\rangle_L, \tag{A3}$$

which is the squared field amplitude averaged over local unit cell. The real electromagnetic energy density $W(z)$ is similar to $|\Psi(z)|^2$. Both of them are strongly oscillating functions of the coordinate z with the period of oscillations coinciding with the unit cell length L. Thus, the quantity (A3) can be interpreted as the smoothed field intensity distribution, with the correction coefficient of the order of unity.

In all plots, the wave number k and the frequency ω are expressed in units of L^{-1} and cL^{-1}, respectively.

[1] A. Yariv and Pochi Yeh, *Optical Waves in Crystals* (Wiley-Interscience, New York, 1984).

[2] Pochi Yeh, *Optical Waves in Layered Media* (Wiley, New York, 1988).

[3] Weng Cho Chew, *Waves and Fields in Inhomogeneous Media* (Van Nostrand Reinhold, New York, 1990).

[4] A. Mell, F. Morichetti and M. Maritelli, Opt. Quantum Electron. **35**, 365 (2003).

[5] A. Mandatori, C. Sibilia, M. Centini, G. D'Aguanno, M. Bertolotti, M. Scalora, M. Bloemer, and C. M. Bowden, J. Opt. Soc. Am. B **20**, 504 (2003).

[6] M. Scalora, J. Flynn, S. B. Reinhardt, R. L. Fork, M. J. Bloemer, M. D. Tocci, C. M. Bowden, H. S. Ledbetter, J. M. Bendickson, J. P. Dowling, and R. P. Leavitt, Phys. Rev. E **54**,R1078 (1996).

[7] M. Bloemer, K. Myneni, M. Centini, M. Scalora, and G. D'Aguanno, Phys. Rev. E **65**, 056615 (2002).

[8] M. Soljacic, S. Johnson, S. Fan, M. Ibanescu, E. Ippen, and J. D. Joannopoulos, J. Opt. Soc. Am. B **19**, 2052 (2002).

[9] J. Poon, J. Scheuer, Y. Xu, and A. Yariv, J. Opt. Soc. Am. B **21**, 1665 (2004).

[10] D. W. Berreman, J. Opt. Soc. Am. A **62**, 502 (1972).

[11] I. Abdulhalim, J. Opt. A, Pure Appl. Opt. **2**, 557 (2000).

[12] I. Abdulhalim, J. Opt. A, Pure Appl. Opt. **1**, 646 (1999).

[13] A. Figotin and I. Vitebsky, Phys. Rev. E **63**, 066609 (2001).

[14] A. Figotin and I. Vitebskiy, Phys. Rev. B **67**, 165210 (2003).

[15] A. Figotin and I. Vitebskiy, Phys. Rev. E **68**, 036609 (2003).

[16] J. Ballato, A. Ballato, A. Figotin, and I. Vitebskiy, Phys. Rev. E **71**, 036612 (2005).

[17] A. Figotin and I. Vitebskiy e-print physics/0504112.

[18] E. Coddington and R. Carlson, *Linear Ordinary Differential Equations* (SIAM, Philadelphia, 1997).

[19] R. Bellman, *Introduction to Matrix Analysis* (SIAM, Philadelphia, 1997).

[20] P. Lancaster and M. Tismenetsky, *The Theory of Matrices* (Academic Press, New York, 1985).

[21] J. Wilkinson, *The Algebraic Eigenvalue Problem* (Oxford University Press, London, 1996).